Applied Surface Science 670 (2024) 160620

Contents lists available at ScienceDirect

Applied Surface Science

journal homepage: www.elsevier.com/locate/apsusc

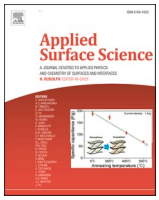

Full Length Article

Enhanced electrochemical performance of partially amorphous $La_{0.6}Sr_{0.4}CoO_{3-\delta}$ oxygen electrode materials for low-temperature solid oxide cells operating at 400 °C

Bartłomiej Lemieszek [a,*], Mindaugas Ilickas [b], Jan Jamroz [c], Asta Tamulevičienė [b], Jakub Karczewski [d], Patryk Błaszczak [d], Alexey Maximenko [e], Brigita Abakevičienė [b], Marcin Małys [c], Sigitas Tamulevičius [b], Piotr Jasiński [a], Sebastian Molin [a]

[a] Advanced Materials Centre, Faculty of Electronics, Telecommunications and Informatics, Gdańsk University of Technology, ul. G. Narutowicza 11/12, 80-233 Gdańsk, Poland
[b] Institute of Materials Science of Kaunas University of Technology, K. Baršausko str. 59, Kaunas LT-51423, Lithuania
[c] Warsaw University of Technology, Faculty of Physics, Koszykowa 75, 00-662 Warsaw, Poland
[d] Advanced Materials Centre, Faculty of Applied Physics and Mathematics, Gdańsk University of Technology, ul. G. Narutowicza 11/12, 80-233 Gdańsk, Poland
[e] National Synchrotron Radiation Centre SOLARIS, Jagiellonian University, Czerwone Maki 98, 30-392, Kraków, Poland

ARTICLE INFO

Keywords:
Solid oxide cells
Oxygen electrode
LSC
Partially amorphous
XAFS
EIS

ABSTRACT

This work evaluates partially amorphous $La_{0.6}Sr_{0.4}CoO_{3-\delta}$ (LSC) as a potential oxygen electrode for low-temperature solid oxide cells. LSC was deposited using the spin-coating technique onto $Ce_{0.8}Gd_{0.2}O_{2-\delta}$ (CGO) substrates. The optimal oxygen electrode thickness was determined as 500 nm. The electrochemical impedance spectroscopy (EIS) study showed a significant improvement in oxygen reduction/oxidation reaction kinetics when annealing temperatures below 600 °C. The lowest value of the polarisation resistance was observed for the sample annealed at 400 °C, followed by a temperature of 500 °C. EIS measurements at different pO_2 content were performed at levels between 0.5 % and 20 %. A comprehensive equivalent circuit analysis was carried out for an explanation of the limiting factors of the catalytic reaction. X-ray absorption fine structure analysis allowed for the identification of differences between crystalline LSC and its partially amorphous form. X-ray absorption near-edge spectroscopy analysis indicated that cobalt adopts a lower oxidation state for the partially amorphous form. Moreover, extended X-ray absorption fine structure analysis indicated the decreased of cobalt oxidation state in partially amorphous LSC. It can be assumed that the increased activity of LSC at temperatures below the crystallization may be due to increased defects and oxygen vacancies in the material.

1. Introduction

Solid oxide cells (SOCs) technology has been continuously developing for decades [1]. This potentially zero-emission technology to obtain energy from hydrogen may be crucial in the process of energy transformation [2]. Initially, the operating temperature of the fuel cells was 1000 °C and above, and it immediately became clear to commercialise the technology, it was necessary to reduce the working temperature and the high operating costs associated with it. Over the last 20 years, it has been provided to reduce the operating temperature of cells to the operating range of 600 °C to 800 °C, and the temperature of 500 °C is increasingly being studied. Reducing the optimal operating temperature for SOCs and increasing the efficiency requires solving many problems. In such a situation, it became necessary to find appropriate materials that allow for a reaction to happen at lower temperatures with high efficiency [1,3].

Recently, much attention has been devoted to the development of high-performance oxygen electrodes for intermediate and low-temperature SOCs applications. Pristine material used as a oxygen electrode was a perovskite material that conducts both electronically and ionically, $La_{1-x}Sr_xMnO_3$ (LSM). However, lowering the operating temperature creates a need for new materials with properties better than LSM. The search for alternatives led to materials such as LSC ($La_xSr_{1-x}CoO_{3-\delta}$) or LSCF ($La_xSr_{1-x}Co_yFe_{1-y}O_{3-\delta}$). Among the materials used as

* Corresponding author.
E-mail address: bartlomiej.lemieszek@pg.edu.pl (B. Lemieszek).

https://doi.org/10.1016/j.apsusc.2024.160620
Received 17 May 2024; Received in revised form 22 June 2024; Accepted 27 June 2024
Available online 30 June 2024
0169-4332/© 2024 The Authors. Published by Elsevier B.V. This is an open access article under the CC BY license (http://creativecommons.org/licenses/by/4.0/).

oxygen electrodes in low-temperature SOCs, one should include $Ce_{0.8}Gd_{0.2}O_{2-\delta}$ (CGO) infiltrated by LSC and LSCF [4]. Other potentially promising materials include praseodymium oxide [5,6], $Pr_2NiO_{4+\delta}$ [6], and strontium-cobalt oxide doped with antimony [7].

Of the materials mentioned, LSC and LSCF currently seem to be the most promising. LSC can exhibits two crystalline forms. Chen et al. examined the crystallographic structure of the LSC and showed the presence of the hexagonal (trigonal, rhombohedral) lattice form in the temperature range from room temperature up to 390 °C. Between 390 °C and 611 °C, there is a phase transition to the cubic perovskite phase, which is stable above 611 °C. In that study, LSC powders were synthesised by a solid-state reaction [8]. The synthesis of LSC usually ends with obtaining a product consisting of several phases, as demonstrated by Hayd et al. The crystallographic analysis of LSC layers deposited on CGO showed, in addition to the perovskite $La_{0.6}Sr_{0.4}CoO_{3-\delta}$ phase, the $(La,Sr)_2Co_{4+\delta}$ and SrO phases [9]. Moreover, Co_3O_4 phase was also detected in other works [10]. The synthesis temperature below 550 °C results in obtaining the material in semi-amorphous or amorphous form [11,12]. LSC is known as a oxygen electrode material with a high ionic conductivity between 0.56 S/m and 1.2 S/m at 700 °C [13,14]. For LSCF, this value is 0.474 S/m at the same temperature [14]. So far, the electrochemical properties of LSC have been mainly studied at temperatures >400 °C, whereas its performance at lower temperatures remains unexplored [15]. Such a low operating temperature also allows the possibility of using amorphous and partially amorphous materials.

In the literature, the vast majority of works refer to crystalline LSC. Limited number of papers undertake research on amorphous LSC. At low temperatures, the best results when it comes to the performance of crystalline electrodes, so far, has been achieved by Kim et al., who obtained polarisation resistance (R_{pol}) value ~1.51 Ω·cm^2 at 400 °C for the oxygen electrode in the form of LSC-LSCF composite, where the LSC was added in the process of infiltration in the form of nanosheets [16]. The infiltration of CGO with LSC was also used by Samson et al. and the research team obtained at the same temperature value of R_{pol} equal to 2.57 Ω·cm^2 [17]. Hayd et al. investigated the use of LSC as a oxygen electrode in their work. The 200 nm-thick oxygen electrode layer was screen-printed. The area specific resistance (ASR) value for the symmetrical half-cell was ~3.2 Ω·cm^2 at 400 °C [9]. Samat et al. presented a oxygen electrode in the form of LSC prepared by the polymeric complexation method. The oxygen electrode thickness used was around 1 μm. At a temperature of 400 °C, the polarisation resistance was approximately 32 Ω·cm^2 [18]. Januschewsky et al. reported the use of LSC as a oxygen electrode deposited on yttria-stabilised zirconia (YSZ) using pulsed laser deposition (PLD), and the selected layer thickness was set at 200 nm. For the layer deposited at a temperature of 420 °C and kept for 3 days at 600 °C, the polarisation resistance was determined in the temperature range of 600–400 °C. At 400 °C, the value of the polarisation resistance was approximately 180 Ω·cm^2 [19].

For amorphous or partially amorphous electrode materials, the number of valuable scientific publications is quite limited. Cavallaro et al. investigated the potential use of an amorphous LSC as a oxygen electrode in low-temperature SOCs. A layer with a thickness of around 300 nm was deposited by the PLD technique and subjected to thermal treatment in the temperature range from room temperature through 200 °C and up to 750 °C. The R_{pol} value at the temperature of 415 °C was as high as 850 Ω·cm^2 [20]. Evans et al., used partially amorphous LSC as a oxygen electrode for micro-solid oxide fuel cells. Oxygen electrode thicknesses were set as 100 nm and 200 nm, and for the latter value at 400 °C, the ASR value for the oxygen electrode was determined to be no more than 0.3 Ω·cm^2 as deconvoluted from fuel cell measurements [12]. Due to limited number of studies, and a wide range of R_{pol} values, the electrochemical performance of amorphous or partially amorphous electrode materials remains interesting for further exploration. In this article, we present and discuss the influence of the LSC structure on the electrocatalytic properties of oxygen reduction/oxidation at low-temperatures.

2. Experimental

The base on which the oxygen electrode layer was deposited was pellets prepared from $Ce_{0.8}Gd_{0.2}O_{2-\delta}$ powder (GDC-20 K or CGO, Daiichi Kigenso Kagaku Kogyo, Japan). 0.8 g of CGO powder was placed in a mould with a diameter of 16 mm and pressed at 98 MPa for 1 min. The prepared pellets were sintered at 1450 °C for 10 h in the box furnace. After sintering, the pellets shrank to an average diameter of 13 mm. The samples were polished on both sides on a semi-automatic polisher (Struers Tergamin-20) and annealed again at 1200 °C for 2 h.

The $La_{0.6}Sr_{0.4}CoO_{3-\delta}$ precursor was prepared in the ethylene glycol photopolymerization process. $La(NO_3)_3{\cdot}6H_2O$ (99.9 % purity, Alfa Aesar), $Sr(NO_3)_2$ (99 % purity, Sigma Aldrich), and $Co(NO_3)_3{\cdot}6H_2O$ (99 % purity, Sigma Aldrich) were dissolved in proper stoichiometry in distilled water to obtain a concentration of 0.25 mol·dm^{-3}. Ethylene glycol (99 % purity, Sigma Aldrich) and citric acid (99 % purity, Chempur) were added to the solution in a mass ratio of 1:1. Additionally,10 wt% of ethanol (99,8% POCH) was added, along with 0.05 wt% of the photoinitiator [2-hydroxy-4′-(2-hydroxyethoxy)]-2-m-ethyl-propiophenone (98 % purity, Sigma Aldrich). When all substrates were mixed, the solution was exposed to UV light for 13 min (a time selected from preliminary studies to determine optimal conditions). UV light was provided by the laboratory ultraviolet lamp EMITA VP-60, rated power 180 W, at a supply voltage of 220–240 V AC. A wood glass filter was used that transmits UV radiation in the range of 320 to 400 nm, with a maximum at 365 nm.

To determine the crystalline or partially amorphous structure at low temperatures, a series of LSC powders synthesised from the described precursor, was prepared and sintered in a furnace for two hours at a temperature ranging from 400 °C to 1000 °C in increments of 100 °C. The product of sintering obtained in this way was ground in a mortar to obtain a homogeneous powder. These samples were analysed by X-ray diffraction (XRD), high-temperature X-ray diffraction (HT-XRD), and XAFS (X-ray absorption fine structure) in XANES (X-ray absorption near-edge spectroscopy) and EXAFS (extended X-ray absorption fine structure) regions.

The LSC oxygen electrode was deposited onto the prepared pellets using the spin-coating technique (Laurell spin coater, model WS-400B-6NPP/LITE). 20 μl of LSC precursor was dropped onto the surface of CGO, and using a three-stage rotational speed, excess solution was removed at 500 rpm for 20 s, 1000 rpm for 20 s, and 3000 rpm for 30 s. After each application of a new layer, the heat treatment process was applied using a hot plate, and the pellets were heated to 400 °C for 15 min. A series of samples with a different number of application cycles, from 1 to 20, were made to determine the relationship between the number of cycles and the thickness of the final layer. It was determined that 10 cycles gave a oxygen electrode thickness of around 300 nm, and 20 cycles resulted in a thickness of around 500 nm. After the predetermined oxygen electrode thickness was reached, the edges of the half-cells were polished to remove the remaining LSC at the edges. Then, they were annealed in the furnace (Carbolyte RHF 16/8 box furnace) in the temperature range of 400–1000 °C for 2 h. The method of sample preparation (multiple heating and cooling cycles) did not cause delamination of the layer from the substrate. After determining the proper thickness layer, still good adhesion with the substrate was achieved. Moreover, further measurements at higher temperatures did not show significant differences in ohmic resistance values over a wide temperature range. A current collector layer in the form of LSC paste (Fiaxell) was applied to each of the pellets and annealed at 400 °C for 2 h. The symmetrical half cells prepared in this way, with the LSC oxygen electrode on both sides, were used for further tests.

The viscosity of the prepared precursor was measured using a FUNGILAB ALPHA series rotational viscometer with an adapter for measuring small samples. 10 ml of the precursor before and after the photopolymerization process was used to perform the measurement. The rotation speed was selected for each sample to ensure the highest

MOST WIEDZY Downloaded from mostwiedzy.pl

accuracy of the measurement indicated by the viscometer.

Wetting properties were probed with drop shape analyser DSA25 (Krüss) under the sessile drop mode. The contour of the 2 μl drop was imaged using dedicated software Advance and fitted with the Young Laplace method.

XRD was used to examine the microstructure of LSC powder samples using a Bruker D2Phaser (Bruker AXS, Mannheim, Germany) diffractometer with a Lynxeye XE-T detector and CuKα radiation (α = 0.15406 nm).

Data for high-temperature X-ray powder diffraction was gathered on a Philips X'Pert Pro diffractometer, equipped with an X'Celerator detector. Ni-filtered Cu-Kα radiation was used to generate the data, and the values for λ_1 and λ_2 were 1.54056 Å and 1.54439 Å, respectively. Measurements at the elevated temperatures were carried out with the assistance of an Anton-Paar HTK 1200 high temperature camera. The LaB_6 standard was used for the calibration process. Diffraction patterns were obtained in air at room temperature as well as at intervals of 50 °C ranging from 50 °C to 850 °C.

Raman spectra were acquired using an inVia spectrometer (Renishaw, United Kingdom) outfitted with an optical microscope (Leica, Wetzlar, Germany) and a motorised sample platform. Using a 50x objective, the excitation beam from a diode laser emitting at 532 nm was focused on the sample. At the surface of the sample, the laser power was 3.2 mW. The Raman Stokes signal was scattered using a diffraction grating with 2400 grooves per millimetre, and the data were captured using a Peltier-cooled charge-coupled device (CCD) detector with 1024 × 256 pixels. This system has a spectral resolution of around 1 cm^{-1}. Silicon was used to calibrate both the Raman wavenumber and the spectral intensity of the Raman apparatus.

Fourier transform infrared (FTIR) spectra were acquired at room temperature using a VERTEX 70 (Bruker, Ettlingen, Germany) spectrometer. Scans were performed in Kubelka-Munk mode in the range of 4000 to 400 cm^{-1}.

The X-ray absorption spectroscopy measurements at the Co K-edge were made at the ASTRA beamline at the SOLARIS National Synchrotron Radiation Centre in Cracow, Poland. The white beam from the 1.3 bending magnet was monochromatized by modified Lemonnier type double crystal monochromator equipped with Ge(220) crystal pair. At the sample position the size of the monochromatized beam was 7x1 mm. The XAFS spectra in XANES and EXAFS regions were collected in transmission mode, where sample chamber and ionisation chambers were filled with N_2 gas at atmospheric pressure. The monochromator at the Co K-edge was calibrated using Co foil from Exafs Company. During the measurements of the samples of interest the Co foil was also measured as a reference sample in order to control alignment of the collected spectra. For the measurements the homogeneous powder of samples of interest were mixed with cellulose and uniform pellets of diameter 1.3 cm were made. To get a good edge step the mass of the powders before mixing with cellulose were evaluated using XAFSmass program. A further analysis of the spectra was performed using Athena and Arthemis softwares. The crystallography data used to fit the calculated Fourier transform (FT) spectra was taken from the Crystallography Open Database (COD). FEFF files for fitting into the Artemis software have been prepared on the WebAtoms website. A map of the intensities of the atom distribution was made using wavelet transforms (WT) with Hama Fortran software [21,22].

Electrochemical impedance spectroscopy (EIS) was used to measure the ohmic and polarisation resistance (R_{ohm} and R_{pol}) of the prepared symmetrical cells (LSC|CGO|LSC) with an excitation amplitude of 25 mV and a frequency range of 3 MHz–50 mHz. The samples were placed in a compression cell where on each side of the sample was a gold mesh electrically connected to platinum wires leading outside the furnace. EIS studies aimed to determine the influence of the material structure (partly amorphous and crystallised) on the catalytic properties. Measurements were performed in an atmosphere of synthetic air with a flow rate of 50 ml·min^{-1}. The tested temperature range varied depending on the annealing temperature. For lower annealing temperatures, more frequent measurements were used to more precisely analyse the low-temperature range.

Measurements at various partial contents occurred at pO_2 values of 0.5 %, 1 %, 3 %, 5 %, 10 %, and 20 % at a flow rate of 50 ml·min^{-1}. Before the measurement, stabilisation in an atmosphere of selected pO_2 for 4 h was done. EIS measurements were performed in the range of 400 °C–300 °C every 25 °C. The Distribution of Relaxation Times (DRT) method was used for detailed analysis. For this purpose, the DRTtool Matlab GUI was used [23]. The DRT analysis was performed by choosing the C4 Matern method of discretization utilizing the 2nd order of the regularization derivative and a regularization parameter (λ) of 10^{-4}.

The samples were aged in an atmosphere of synthetic air, where pO_2 is 20 %, and in isothermal conditions at a temperature of 400 °C. Measurements were carried out for 100 h, with collecting spectra every 5 h.

3. Results and discussion

3.1. Layer preparation and structural analysis

The preparation of the oxygen electrode layer began with the preparation of the precursor. In this case, instead of the standard precursor prepared by the Pechini patent [24], the photopolymerization process was used. The increase in viscosity from 50.6 mPa·s to 88.88 mPa·s indicates that the use of a photoinitiator and UV light accelerated the polymerization process of ethylene glycol (EG) to polyethylene glycol. Contact angle analysis was used to see how the wettability changed and to compare it with the EG-based solution that was made as described above (S1 and S2 in the supplementary). In the case of distilled water, the initial contact angle was around 60° and gradually decreased to reach the minimum measured angle of approximately 7° after approximately 12 min. In the case of the EG-based reference solution, the initial value of the contact angle was around 20°, and after 6 min, it dropped to approximately 5°. As expected, the prepared precursor had an initial contact angle lower than before photopolimerisation and the value was about 20°. However, the CGO surface was much more wettable, so after two to three minutes, the contact angle became too small to measure. Contact angle measurements indicate that the new precursor preparation method accelerates the wettability of the CGO surface.

Fig. S3 shows the SEM images of the LSC layers deposited on the CGO surface using the spin-coating technique with a varying number of deposition cycles. The average LSC layer thicknesses from the SEM images were ~50 nm, ~100 nm, ~190 nm, ~230 nm, ~290 nm, and ~500 nm for 2, 4, 6, 8, 10, and 20 cycles respectively. Fig. S4 presents the calibration curve for oxygen electrode layer deposition depending on the number of cycles.

Fig. 1A shows the XRD results of the LSC powders sintered at different temperatures. It shows that the diffractograms have characteristic peaks that correspond to both R$\underline{3}$c rhombohedral phases. These are the main peaks at 33° (110, 104), 47.5° (113), and 58° (024). However, there were also peaks indicating the $Pm\bar{3}m$ phase at 23.25° (012) and 40.75° (202). At 600 °C, in addition to the main peaks, characteristic of strontium carbonate became visible at 25.5° and 36° as well as faint peaks at 45° and 50°. The presence of strontium carbonate as an impurity is typical for LSC materials [25]. Below the temperature of 600 °C, the diffraction pattern indicates a partially amorphous form of the analysed material. LSC-specific peaks are noticeable and recognisable. In addition, peaks at 31.3° and 65.2°, not present at higher temperatures, were observed, indicating the presence of Co_3O_4.

Fig. 1B shows the Co K-edge XANES spectra for the LSC material as a function of annealing temperature. At around 7709 eV in each of the LSC samples, the pre-edge feature is observed, regardless of the annealing temperature. For 3d metals, the pre-edge feature depends on the contribution of the 1 s electric dipole transition to the 4p component in 3d – 4p hybridized orbitals and the tiny quadrupole transition to 3d

MOST WIEDZY Downloaded from mostwiedzy.pl

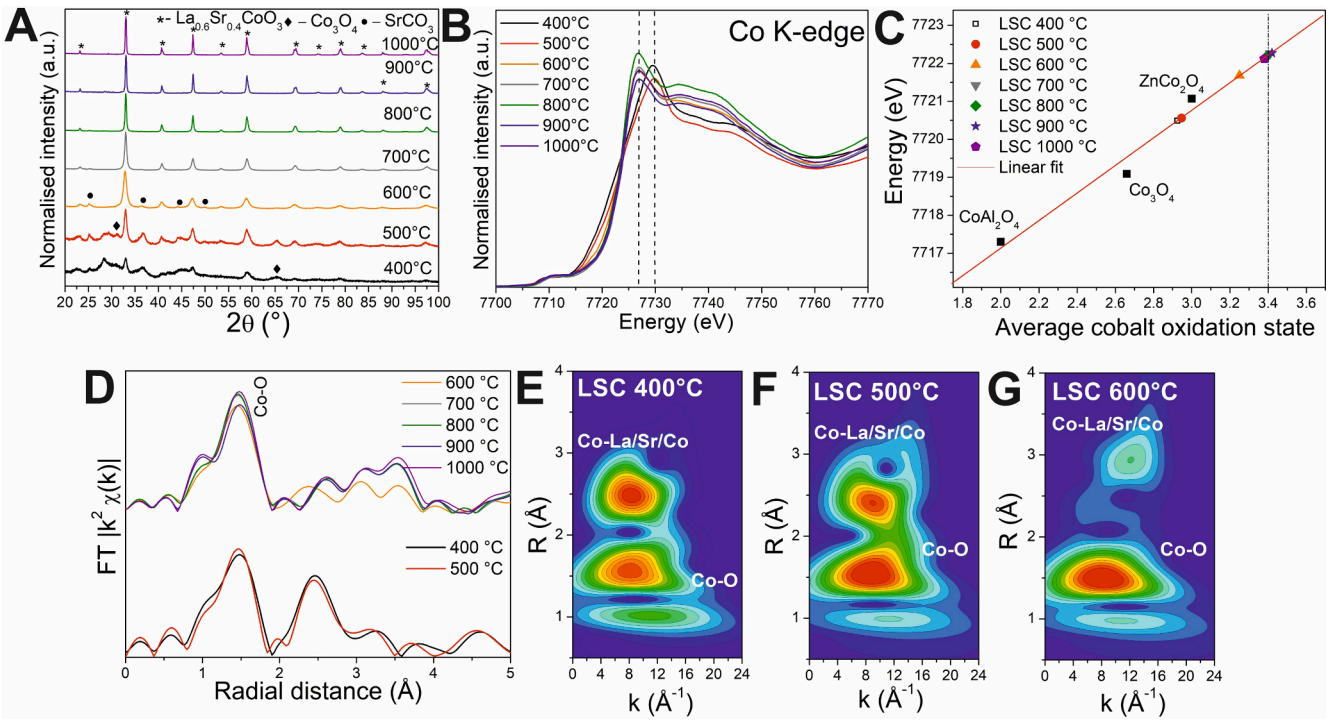

Fig. 1. X-ray diffraction of LSC powders annealed at different temperatures (A); XANES spectra (B); Average cobalt oxidation state calculated from mid-energy (C) R-space FT Fourier transform (k2χ(k)) Co-K-edge EXAFS for LSC as a function of annealing temperature (D); and Wavelet Transform calculated from EXAFS for LSC annealed at range 400 °C–600 °C (E-G).

component. The p-d hybridization could not occur for a regular octahedral symmetry, and the pre-edge peak is weak because the transition momentum of the electric quadrupole process is small. When the center of inversion symmetry is broken due to progressive distortion from octahedral to tetrahedral geometry, the pre-edge feature gains additional intensity due to the 1 s transition to the 4p component in the 3d–4p hybridized orbital, where the mixing of 4p and 3d depends strongly on the coordination symmetry [26]. In this case, the pronounced pre-edge peak for LSC could be explained by distortions of the octahedral structure due to the occurrence of defects and oxygen vacancies. Additional distortions introduced by the lack of a fully crystalline structure only increase the level of distortion, resulting in a distinct pre-edge peak [27,28].

Fig. 1C presents a linear relationship between the cobalt oxidation state and the mid-edge energy. It should be noted that the choice of the edge position is rather arbitrary, therefore the value of mid-egde energy was chosen to verify the spectral shift. In order to determine the curve determining this relationship, standard compounds with known and established oxidation states were used. The XANES spectra indicate the presence of cobalt is close to the theoretical value of 3.4^{+}, so therefore, cobalt occurs in both 3^{+} and 4^{+} oxidation states in LSC annealed above 600 °C. The situation was different for LSC annealed below 600 °C. The lower the annealing temperature, the more a more a gradual decrease in the average oxidation state of cobalt is observed. At a temperature of 600 °C, this value is already $\sim 3.3^{+}$; at annealing temperatures of 500 °C and 400 °C, it is 2.9^{+}. The decrease in the average oxidation state of the cobalt in the LSC structure significantly affects the properties of the material itself. Fig. 1D shows k-space oscillation plots and Fourier transform (FT) (k2 χ(k)) plots of EXAFS for LSC annealed at different temperatures (no phase correction were applied). In the obtained spectrum, the first peak reaches its maximum at a radial distance of approximately 1.5 Å. This peak occurs for both partially amorphous and crystalline structures. In non-crystalline LSC, a peak at approximately 1.1 Å is also visible, the intensity of which in the crystal structure is much lower. In the case of partially amorphous structures, the next peak is observed at a radial distance of ~2.5 Å. This is a significant difference from the crystal structure, where the three broad peaks indicate Co-Sr/La/Co is in the range of 2.7–3.8 Å. Figs. S6A and S6B present the LSC spectra and the results of fitting the vibrational spectra $|X(R)|$ ($Å^{-4}$) in k-space and k^3 X(k)($Å^{-3}$) in q-space. The parameters obtained during fitting are presented in Table S1. The EXAFS analysis indicates a significant decrease of number of oxygen atoms around the central atom for partially amorphous LSC. For annealing temperatures below 600 °C, the value of the coordination number is close to 4, and for crystalline samples it oscillates between 4.6 and 5.0. The decrease in this value for annealing temperatures of 900 °C and 1000 °C may be related to the formation of additional phases. They may not be visible in the diffractogram, as shown in work Zhang et al., where the formation of the CoO_x phase was not detected using XRD and its occurrence was observed using SEM-EDS. They also determined the stability phase diagrams for $(La_{0.6}Sr_{0.4})_{0.99}Co_yO_{3-\delta}$, and for temperatures above 800 °C in air, the occurrence of LSC with spinel $(La,Sr)CoO_4$ is possible, and above 900 °C, LSC with halite CoO is observed [29]. To better understand the differences between crystalline and partially amorphous material, a wavelet transform (WT) based on Morlet wavelets ($\kappa = 15$, $\sigma = 1$), was also performed for each analysed sample as a function of the annealing temperature. The WT determines the centres of the backscatter wave functions in energy (or wave vector) space. This method is particularly helpful when their waves cannot be separated by the Fourier transform/backtransform approach due to the presence of several elements in one shell, or the irregular nature of the material. Moreover, this method is particularly useful in determining minor changes in the centres of wave functions depending on various factors. Fig. 1 E–G present the obtained maps for annealing temperatures from 400 °C to 600 °C, and Fig. S6 C–F presents the obtained maps for annealing temperatures in the range of 700–1000 °C. For crystalline LSC, there are two areas with maximum intensities at R around 1.5 Å and 3 Å. The first of them corresponds to the Co–O bond and has a quite wide range. The second area originates from the Co-La/Sr/Co. Similar results were observed for all temperatures above 600 °C. In the case of the annealing temperatures of 900 °C

MOST WIEDZY Downloaded from mostwiedzy.pl

and 1000 °C, changes was observed in oxygen occupancy. It may be related to a new phase formation in the LSC at a high temperature [29]. For partially amorphous LSC a clear leftward shift is observed for Co-La/Sr/Co scattering path, where maximum intensities are observed at 2.5 Å, compared to 3 Å for the crystalline LSC. At an annealing temperature below 600 °C, two distinct areas with comparable intensities are observed, which distributions are broader, than for crystalline LSC. Based on the determined values of coordination numbers for Co-O bonds, it can be assumed that the number of oxygen atoms near the central atom has decreased, and may be comparable to the number of cations. This suggests that it can contribute to the occurrence of many more defects in the material itself. The appearance of defects in the structure of the material is related to its activity. Wang et al. analysed the LSC-Co_3O_4 composite in the context of oxygen activation in the material structure. The presence of an interface composed of LSC-Co_3O_4 increases the conversion of inactive oxygen species O^{2-} to active O^{2-x}. This is done by increasing the number of electrons transferred from the perovskite LSC to the Co_3O_4 lattice [30]. The occurrence of such defects may have a beneficial effect on the electrochemical reaction.

Fig. S5A shows high-temperature XRD analysis (HT-XRD) for the powder annealed at 400 °C (amorphous form). The characteristic first peaks of $La_{0.6}Sr_{0.4}CoO_3$ appear at a temperature of 550 °C, which indicates that the minimum temperature for the formation of the LSC perovskite crystal form is between 500 °C and 550 °C. In the temperature range of 550–600 °C, the characteristic $SrCO_3$ peaks are visible. Above 611 °C, a stable perovskite structure is observed, as shown in the literature [8]. The measurements reveal that LSC annealed at temperatures below 550 °C is partially amorphous and will be taken for future examination. To further improve the understanding of the structural properties, the examination with additional is required to offer more accurate details.

Raman spectroscopy was performed on oxygen electrode layers deposited on CGO pellets, and the results are shown in Fig. S5B. Measurements were made for a pure CGO pellet and an LSC layer with a thickness of 500 nm in the range of annealing temperatures from 400 °C to 1000 °C. For the pure CGO pellet, a broad and intensive band was observed with a Raman shift of 470 cm^{-1}. This is the only band observed in the analysed range of the measurement. Raman shift bands for the LSC are visible at 480 cm^{-1}, 520 cm^{-1} and 678 cm^{-1}. At the annealing temperatures of 400 °C and 500 °C, no band at 520 cm^{-1} was observed. In the case of perovskites, the presence of bands in Raman spectroscopy corresponds to Jahn-Teller distortions. In contrast to the perovskite's ideal structure, these distortions cause structural disturbances in the oxygen sublattice structure. Specifically, they cause the differences in the lengths of the Co-O bonds in the octahedral CoO_6, which leads to the formation of a monoclinic structure. In the case of a material such as LSC, strontium doping causes a decrease in the intensity of the bands and their broadening. These bands may be related to the Co^{3+} intermediate spin state [31]. There is a limited number of articles in the literature that even partially deal with the study of Raman scattering of perovskites such as $LaCoO_3$, and in the case of LSC, finding such studies is even more difficult. In the case of the $LaCoO_3$ perovskite, Ishikawa et al. observed Raman bands at 425 cm^{-1}, 536 cm^{-1} and 653 cm^{-1} (relative to the measurement range presented here), but only 425 cm^{-1} for $La_{0.7}Sr_{0.3}CoO_3$ [32]. In the case of $La_{1-x}Sr_xCoO_3$, the Raman shifts were different depending on the grain size and the stoichiometry of the material. Orlovskaya et al. for $La_{0.8}Sr_{0.2}CoO_3$ distinguished shifts of 448 cm^{-1}, 557 cm^{-1} and 673 cm^{-1} [33] and Li et al. for $La_{0.8}Sr_{0.2}CoO_3$ (grain size 11.5 nm) observed shifts at 500 cm^{-1} and 630 cm^{-1} [34]. Celikbilek et al. for $La_{0.6}Sr_{0.4}CoO_3$ he observed bands at 420 cm^{-1} and 678 cm^{-1} [31].

The lack of agreement in the literature regarding the specific bands responsible for LSC makes the analysis of the results even more complex. In this case, $La_{0.6}Sr_{0.4}CoO_3$ overlaps the band at 678 cm^{-1} with the Celikbilek work, and it is also seen that the band at 420 cm^{-1} cannot be determined due to CGO. The band at 500 cm^{-1} was observed in $La_{0.8}Sr_{0.2}CoO_3$ and in $LaCoO_3$ at 536 cm^{-1}, 557 cm^{-1} or 570 cm^{-1} [7]. Aakib et al. showed the presence of Raman bands at 470 cm^{-1}, 510 cm^{-1}, 610 cm^{-1} and 670 cm^{-1} for Co_3O_4 [35].

Fig. S5C shows the FTIR spectra of LSC deposited on CGO pellets and sintered at different temperatures. Bands at wavenumbers 400 cm^{-1}, 562 cm^{-1} and 660 cm^{-1} are recognised. The observed bands at about 400 cm^{-1} and 660 cm^{-1} are attributed to the modes of deformation and stretching vibrations in the plane of the O–Co–O bonds. In addition, the band width at 400 cm^{-1} may indicate the overlapping of the La–O and Sr–O bond stretching vibrations. The vibrations occurring at 562 cm^{-1} can be attributed to the stretching vibrations of the La/Sr–O–Co bonds. At low annealing temperatures, the bands are hardly visible, probably due to irregularities in the surroundings of the analysed bonds, which also affect the shift of the absorption maximum (local minimum of transmittance). The most sharp and visible bands are for LSC annealed at 1000 °C. The values of the wavenumbers that have been matched to the appropriate vibrations correspond to the data from the literature. The FTIR spectra obtained by Ghorbani-Moghadam et al. showed the bands and types of vibrations for the spinel material $La_{0.7}Sr_{1.3}CoO_4$ and the Cu/Fe dopants. They identified three distinct bands at the wavenumbers of 400 cm^{-1}, 520 cm^{-1} and 600 cm^{-1}, respectively. They attributed the first and last bands to stretching vibrations in the plane of the Co(Fe/Cu)-O bonds, and the band between 450–550 cm^{-1} to stretching vibrations of the apical La/Sr-O(II)–Co–(Fe/Cu) bond [36]. In another study, they studied a series of spinels with the $La_{2-x}Sr_xCoO_4$ structure. In the case of $La_{1.3}Sr_{0.7}CoO_4$, bands at wavelengths of 421 cm^{-1}, 486 cm^{-1}, 616 cm^{-1} and 672 cm^{-1} were determined. It was also shown that this band shifted to lower wavenumber values with the change of the La:Sr ratio, and at the La:Sr ratios of 0.9:1.1 and 0.7:1.3, this shift reached the minimum value of 468 cm^{-1} (from 512 cm^{-1}) [37]. In this study, the content of lanthanum and strontium in the perovskite structure is much lower, so it is possible that stretching of the octahedral CoO_6 is present, but it is invisible, or it consists of a wide band from 400 cm^{-1} to as much as 480 cm^{-1}. Sivakumar et al. identified bands at 446 cm^{-1}, 476 cm^{-1} and 620 cm^{-1} for the $LaCoO_3$ perovskite. They determined that at 446 cm^{-1}, can be attributed to the La-O stretching, and at 620 cm^{-1} for O-Co-O stretching vibrations. Mishra et al. analysed the $LaCoO_3$ material and identified the band at 586 cm^{-1} as stretch vibration between Co-O-Fe/Ni-O, as well as vibrations in the octahedral perovskite structure [38]. Garces et al. performed the FTIR spectroscopy measurement for the $LaSrCoO_3$ perovskite. In the spectrum, they identified bands at wavenumbers of 686 cm^{-1} and 523 cm^{-1}. The band at 686 cm^{-1} was related to the O-Co-O bond stretching vibrations, and the band at 523 cm^{-1} is related to the La-O and Sr-O bond stretching vibrations [39]. The occurrence of the described bands for each annealing temperature indicates the similar nature of the crystalline and partially amorphous material. The decrease in band intensity with decreasing annealing temperature is also noticeable and indicates the presence of a more disordered structure.

SEM images in Fig. 2A–G depict the surface morphology of the oxygen electrode. At an annealing temperature of 400 °C, the grains are too small (<10 nm) to distinguished. The grain size was ~23 nm at the annealing temperature of 500 °C. The average grain sizes for crystalline LSC were around 40 nm, 68 nm, 82 nm, 147 nm, and 112 nm at annealing temperatures of 600 °C, 700 °C, 800 °C, 900 °C, and 1000 °C, respectively. There is also a considerable increase in the pore size. The pore size of a partially amorphous LSC is nanometric and grows as the annealing temperature increases. During high annealing temperatures, the pores expand to a size larger than the grains.

3.2. Electrochemical impedance spectroscopy

Structural analysis indicated differences between crystalline and amorphous LSC. These differences may affect the catalytic properties of the material. To determine the efficiency of the electrochemical oxygen electrochemical reaction, various types of measurements were carried

MOST WIEDZY Downloaded from mostwiedzy.pl

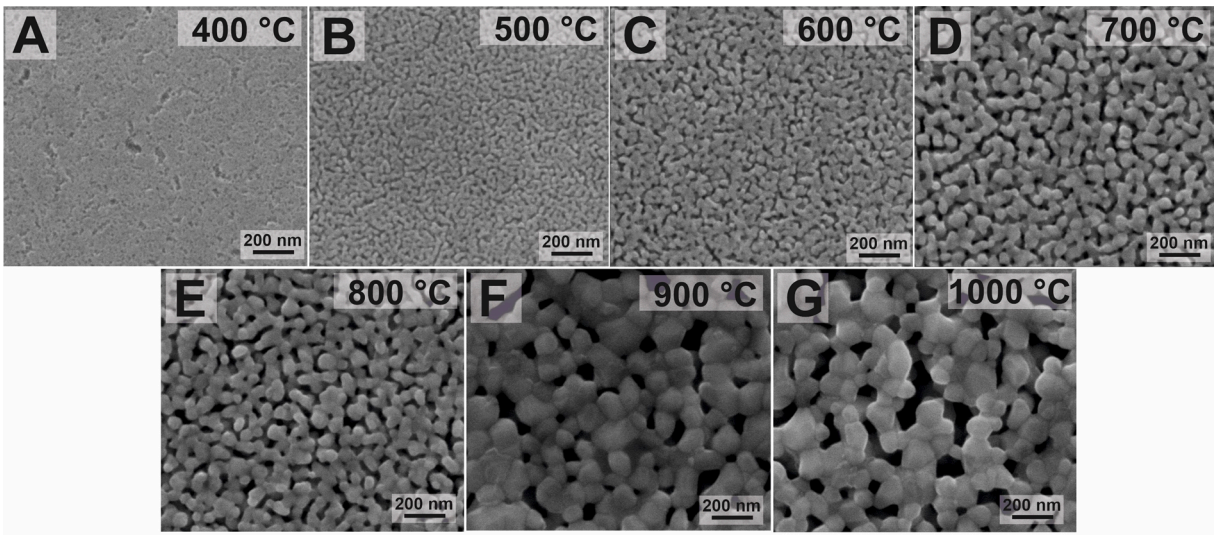

Fig. 2. SEM images of the LSC-based oxygen electrode surface depending on different annealing temperatures: from 400 °C to 1000 °C (A-G).

out using electrochemical impedance spectrometry. The value of polarisation resistance (R_p or R_{pol}) was taken into account as a key parameter for assessing the efficiency of this process. A series of symmetrical samples was prepared for the tests.

3.2.1. *Optimal thickness determinations*

The first stage of the research using EIS was to determine the optimal thickness of the LSC layer, starting at 200 nm and ending at 1000 nm. The electrochemical performance, depending on the thickness, was determined in the temperature range of 400 °C–300 °C by performing three impedance measurements every 25 °C. Fig. 3A and 3B show the ohmic and polarisation resistances, and Fig. 3C shows the obtained impedance spectra for various oxygen electrode thicknesses. At 400 °C, values of polarisation resistance of 59.3 Ω·cm^2, 38.8 Ω·cm^2, 35.9 Ω·cm^2, and 51.6 Ω·cm^2 were obtained, respectively, for layer thicknesses of 200 nm, 300 nm, 500 nm, and 1000 nm. For the sample without LSC layer (reference sample), this value is 527 Ω·cm^2. The nanoporous LSC oxygen electrode causes a significant increase in the oxygen electrode-air

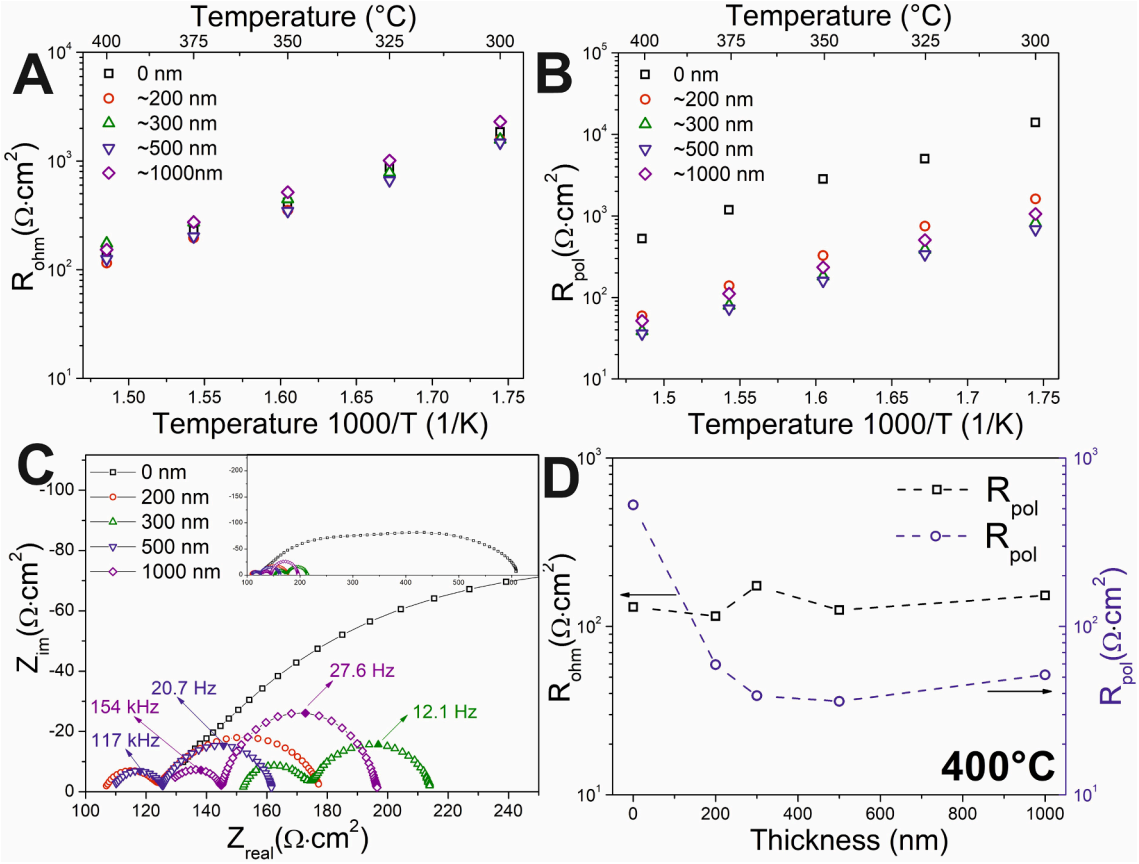

Fig. 3. Influence of $La_{0.6}Sr_{0.4}CoO_{3-\delta}$ oxygen electrode thickness on ohmic (A), polarisation resistance (B), obtained impedance spectra (C), and the relationship between annealing temperature and ohmic and polarisation resistance (D).

MOST WIEDZY Downloaded from mostwiedzy.pl

contact area, which is reflected in the value of the polarisation resistance of the cell. The initial decrease in the polarisation resistance value is related to the increase in the area of the active oxygen electrode layer and more efficient electrochemical reaction. The R_p values for the thickness of 300 nm are close to the sample thickness of 500 nm, and the positive effect of the increase in the active surface is inhibited. At a thickness of 1000 nm, an increase in the R_{pol} value was observed. This might be because the limiting charge transfer through the electrolyte layer. It may become more significant as the thickness of the oxygen electrode increases. Moreover, it can be assumed that the optimal range of oxygen electrode thickness is from 200 nm to 1000 nm. Fig. 3D shows the changes in the values of ohmic resistance and polarisation resistance as a function of electrode thickness. The visible decrease in the R_{pol} value with an increase in electrode thickness is noticeable. This trend is stopped when the thickness is higher than 300 nm, and the lowest value is achieved for a thickness of 500 nm. For the R_{ohm} the values are similar, and no significant effect is noticed. Therefore, a thickness of 500 nm was selected for further research.

3.2.2. *Effect of annealing temperature*

The next stage of the analysis was to assess of the effect of the annealing temperature on the efficiency of the catalytic reaction. This parameter has been proven to have a significant impact of electrode performance [40]. This is due to, among others, the formation of a crystal structure as well as changing the grain size, which directly affects the active surface area.

Fig. 4A shows the ohmic resistance values, Fig. 4B shows the polarisation resistances, Fig. 4C shows the impedance spectra, and Fig. 4D shows the influence of the annealing temperature on the ohmic and polarisation resistance values. The sample annealed at 1000 °C and 800 °C revealed the smallest R_{ohm} values, 78.3 Ω·cm^2 and 82.2 Ω·cm^2 respectively. For other samples, the difference in R_{ohm} value was negligible. Such values for the R_{ohm} parameter indicate that a good bond with the CGO substrate has been achieved. The highest R_{ohm} value at 400 °C was observed of 125 Ω·cm^2 for the sample annealed at 400 °C, followed by the sample annealed at 900 °C with R_{ohm} equal to 117 Ω·cm^2 at the same temperature. Polarisation resistance gives information on the efficiency and activity of the reaction between $La_{0.6}Sr_{0.4}CoO_{3-\delta}$ and O_2. The lowest value was observed for the sample annealed at 400 °C and the highest at 900 °C. These values are respectively 35.9 Ω·cm^2 and 2370 Ω·cm^2 at 400 °C. A significant decrease in polarisation resistance is the result of the nanoporous structure of a partially amorphous $La_{0.6}Sr_{0.4}CoO_{3-\delta}$. A promising result was also obtained for the sample annealed at 500 °C, where the R_{pol} value at 400 °C was 112 Ω·cm^2. The advantage of using partially amorphous LSC is revealed here. The results for fully crystallised LSC are similar, and the best results with crystalline LSC were observed at an annealing temperature of 600 °C. This is influenced by the small grain size of the crystalline LSC, whose active surface is larger compared to LSC annealed at higher temperatures. This effect has been described in previous works [40–42]. The use of a sintering temperature below the formation temperature of a crystalline structure contributes to a significant decrease in the R_{pol} value. This means that the oxygen electrode's activity got enhanced.

Fig. 4D shows the influence of annealing temperature on the ohmic resistance and the polarisation resistance. The results shows the differences in the parameters describing the oxygen electrode, and indicates the optimal parameters. There is a visible downward polarisation resistance with lowering the annealing temperature. For the ohmic resistance, there is a clear indication of a decrease of this parameter with the increase in the annealing temperature. Moreover, activation energy

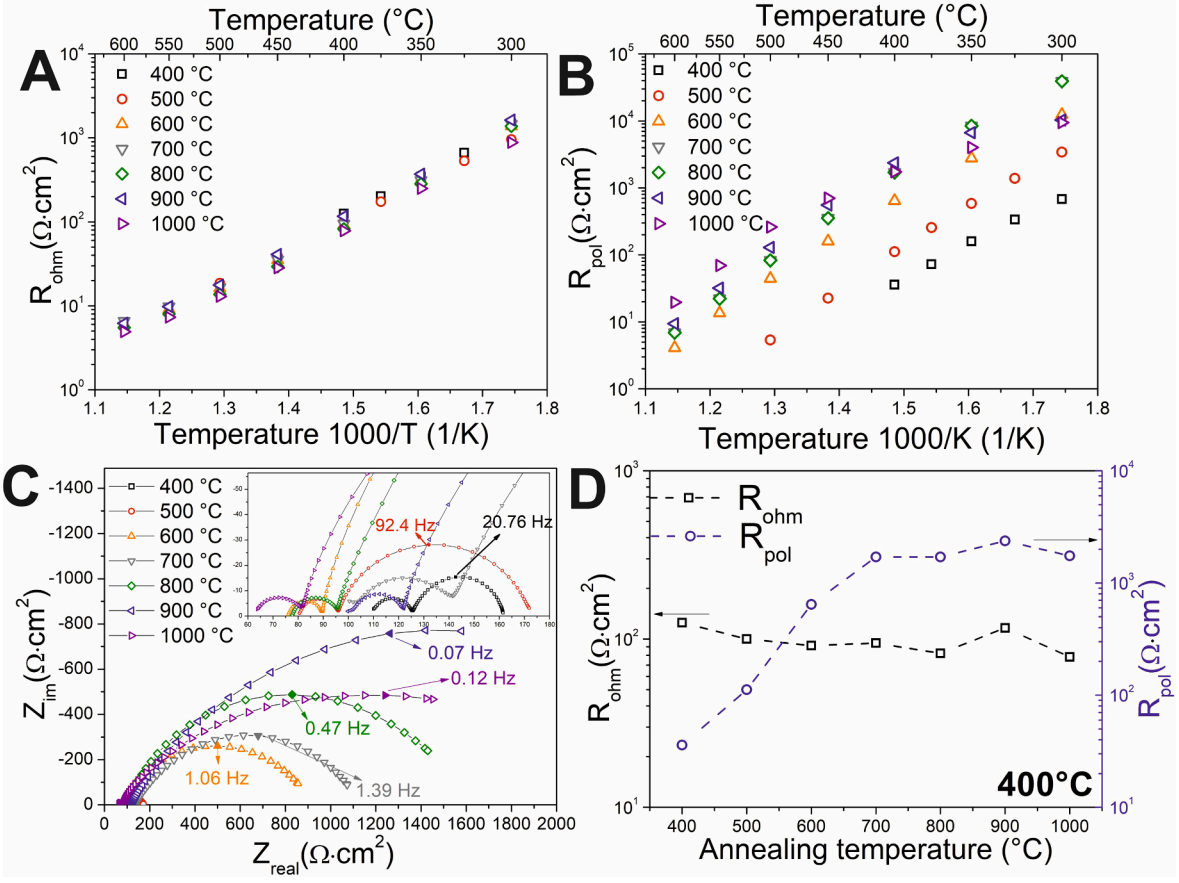

Fig. 4. Ohmic (A) and polarisation (B) values of symmetrical half-cells as a function of annealing temperature; obtained impedance spectra (C), and ohmic resistance and polarisation resistance changes in a function of annealing temperature (D).

MOST WIEDZY Downloaded from mostwiedzy.pl

for the annealing temperature of 400 °C is lower than that calculated for crystalline form (in this case compared to the annealing temperature of 600 °C), and it takes a value of 0.99 eV compared to 1.15 eV. This phenomenon was also described by Cavallaro et al. with amorphous LSC [20].

Additionally, analysing the Bode plots for partially amorphous and crystalline LSC presented in Fig. S7, they show significant differences. A significant reduction in the middle frequencies was observed for the partially amorphous material, as well as a small change in the frequency characteristic of R_{pol} towards higher frequencies. It follows that the reaction mechanism does not differ much in relation to the crystal structure. Obtaining a low R_{pol} value compared to other works describing amorphous materials indicates that the problem of electron migration resistance from the current collector to the active reaction site is avoided. Additionally, the relationship obtained during EIS measurements at different pO_2 resembles the relationship obtained in work on crystalline form of the LSC [40].

Obtaining the best result for the annealing temperature of 400 °C indicates that the presence of an irregular structure with a significant number of defects has a positive effect on the catalytic activity. According to XANES and EXAFS analyses using WT, there may be variations in the arrangement of atoms in the material that could have an impact on the electrochemical efficiency of the material. The possible occurrence of a mixture of LSC with Co_3O_4, as indicated by XRD and Raman spectroscopy and supported by the literature, indicates the superior properties of an partially-amorphous material [30].

3.3. *Detailed electrochemical impedance spectroscopy investigation of electrode processes*

The measurements performed using EIS gave only a partial answer to the question of the effectiveness of the oxygen electrode material. In order to better understand the phenomena that occur in the partially amorphous LSC, a series of measurements were performed at different pO_2 in the temperature range of 400 °C–300 °C. Fig. 5A show obtained impedance spectra, and 5B-C show the ohmic and polarisation resistance values obtained for the measurements at different partial pressures of oxygen. Fig. 5D and 5E show the DRT analysis performed for these

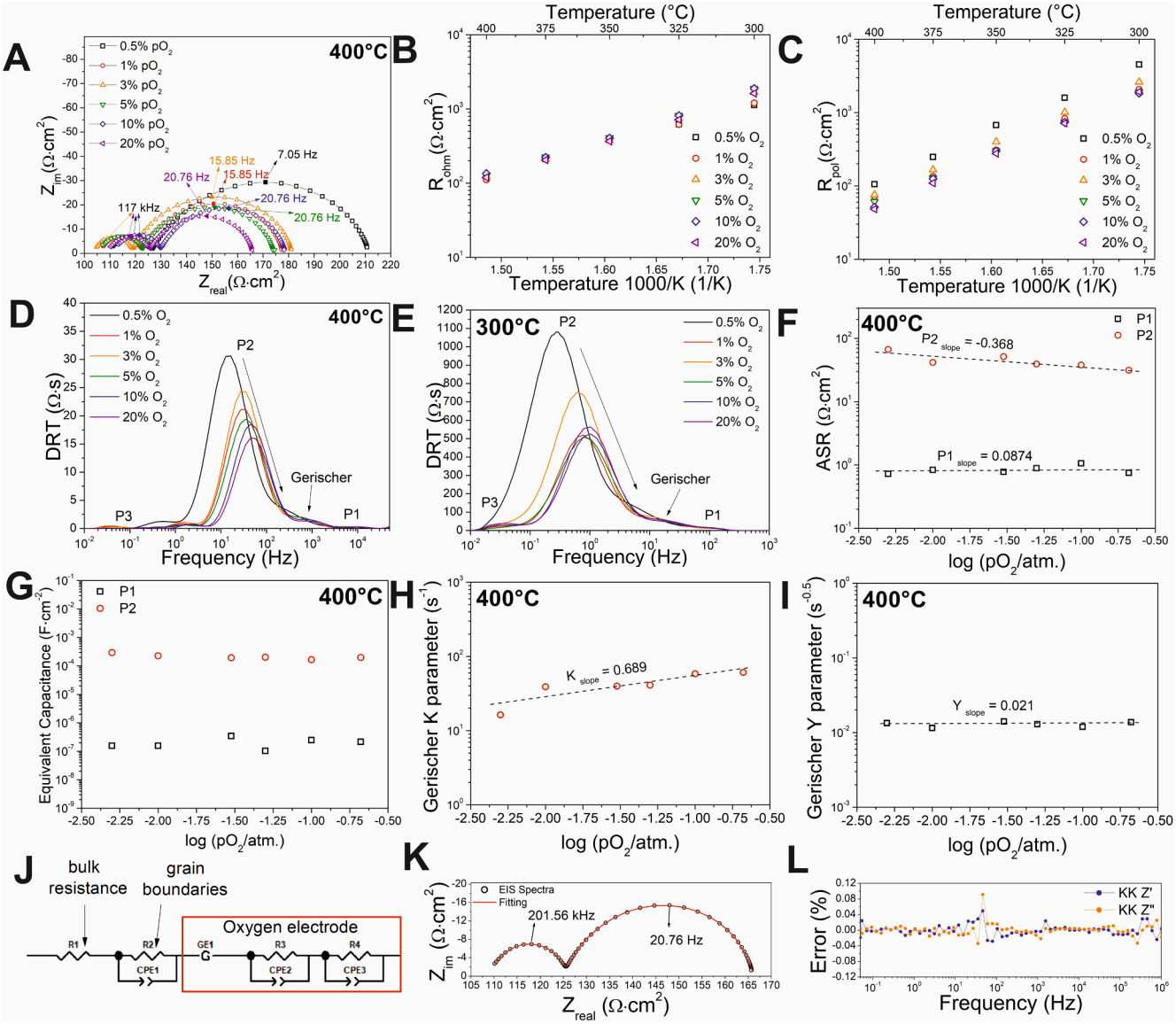

Fig. 5. Impedance spectra obtained during a measurements (A); Arrhenius plots for ohmic (B) and polarisation (C) resistance for measurements at different partial pressures of oxygen and DRT analysis for measurements made at 400 °C (D) and 300 °C (E); determined ASR values for processes P1 and P2 (F), equivalent capacitance values for (G) measured at 400 °C; determined 'K' (H) and 'Y' (I) parameters value for Gerischer element; determined equivalent circuit (J) representative example of fitting for impedance spectra collected in synthetic air (K) and Kronig–Kramers analysis result comparison (L).

MOST WIEDZY Downloaded from mostwiedzy.pl

measurements. According to the available literature analysing DRT at higher temperatures, three processes can be distinguished [40,43]. The decrease in the pO_2 leads to a modest increase in P1 peak area. Furthermore, the area of the P1 process peak grows as the temperature decreases. In comparison to the high frequency range, this behaviour can be attributed to charge transfer at the electrode/electrolyte contact. The P2 process, which occurs in the medium frequency range, is highly dependent on pO_2 and temperature. P2 can be linked to a variety of electrode processes known as surface oxygen exchange kinetics and oxygen ion diffusion, including adsorption of oxygen gas O_2, dissociation of O_2, and charge transfer diffusion (O_2) [44,45]. The final subprocess, P3, occurs at low frequencies and is strongly dependent primarily on pO_2, with peak area increasing as pO_2 decreases. This mechanism is similar to gas diffusion in the porous oxygen electrode and is only marginally temperature-dependent but substantially dependent on microstructural characteristics [46]. Therefore, it is clear that these phenomena are purely thermally activated.

DRT analysis revealed three peaks typical of oxygen electrodes, denoted as subprocesses P1, P2, and P3. Moreover, at higher frequencies, a characteristic is observed indicating the presence of the Gerischer element, which determines mass transport in the electrode. The impedance of the Gerisher element results from the relation:

$$Z(\omega) = \frac{1}{Y(k + j\omega)^{0.5}}. \quad (1)$$

where 'k' is the effective transfer rate of the chemical reaction and 'Y' is the initial coefficient, i.e. the inverse of Z_0 [47]. Variations of the ASRs of the identified electrode subprocesses with pO_2 are shown in Fig. 5F–G. The slope of the curves helps to deduce the likely mechanism of the reaction occurring in the electrodes [48]. The dependency can be attributed to adsorption and surface exchange for slopes 0.5 to 0.25, but a slope of 1 involves the contribution of molecular oxygen and is attributed to gaseous diffusion [49]. For different oxygen concentrations at 400 °C, we observed a slope of 0.087 for process P1 and −0.368 for process P2. It was impossible to analyse the value for the P3 process with the indicated gas diffusion. The reason for that is the low temperature of the experiment, when part of the impedance spectra describing this process is negligible, and it was impossible to achieve proper and valid results. Processes P2 and P1 have different slopes, which may indicate oxygen surface exchange kinetics and oxygen ion diffusion, respectively. In the case of the P1 process, we are talking rather about the charge-transfer reaction at the interface, which has a higher resistance compared to other subprocesses.

The observed capacitance values do not change significantly with increasing oxygen content in the analysed samples. Values observed for the P2 process indicate that it could be the adsorption process [40,45]. In this case, there is no dependence or very small dependence of the capacitance on the oxygen concentration. Capacitance values decrease with increasing oxygen concentration, which correlates with literature data [40,49]. For the P1 process, the capacitance values were $\sim 10^{-7}$ F·cm^{-2}. This is likely because of the charge transfer that occurs at the interface between the electrode and the electrolyte layer. Fig. 5H–I present the determined values of the parameters 'k' and 'Y' for the Gericher element. Examining the impact of oxygen partial pressure on the Gerischer element parameters, a pronounced reliance on the rate constant parameter k (with a slope of 0.689) becomes apparent. Conversely, the Y parameter associated with admittance appears unaffected by changes in pO_2, displaying a nearly constant value with a very small slope. Notably, the resistance of the Gerischer element at 400 °C and pO_2 of 20 % measures 9.3 Ω·cm^2 and exhibits dependency on pO_2. Fig. 5J shows the equivalent circuit obtained by DRT analysis. Fig. 5K shows a representative example of the fit obtained for the equivalent circuit used. Additionally, a Kronig–Kramers (KK) analysis was performed [50,51]. Representative analysis results are presented in Fig. 5L. For most of the spectrum, the relative error of both the real and imaginary data was under 0.04 %.

3.4. Stability tests

The use of a low annealing temperature and the use of partially amorphous $La_{0.6}Sr_{0.4}CoO_{3-\delta}$ can affect the stability of the oxygen electrode over time. The active surface of the electrode may also change. Nyquist plots show the changes over time and are presented in Fig. 6A. Fig. 6B and C show the change of R_{ohm} and R_{pol} parameters over time. In the case of R_{ohm}, an initial value of 92.8 Ω·cm^2 was observed, and the value fluctuated around this value. The final value was 92.3 Ω·cm^2, which means a reduction of 0.5 Ω·cm^2. In the case of the polarisation resistance, an increase in the value from the initial value of 35.7 Ω·cm^2 to the value of 43.2·Ω cm^2 was observed, which means a change in degradation rate of 21 % in 100 h. The observed increase in polarisation resistance is also different from that observed for the crystalline form of LSC at higher temperatures [40,52]. This may be related to various processes, mainly chemical and not necessarily related to degradation, occurring in the partially amorphous material.

Fig. S8 shows the XRD spectra taken on the samples after EIS measurements. Along with the LSC-matched peaks, which were the same as for the powders in the first part of this article, CGO peaks at 29° and 57° and overlapping LSC peaks at 33° and 48° were also found. Moreover, starting from an annealing temperature higher than 600 °C, the occurrence of additional peaks was identified, which indicate the formation of an additional phase adapted to the presence of cobalt spinel at 32°, 37°, 54°, and 66°. At lower temperatures, crystallisation occurs slowly, and the SRN (signal-to-noise ratio) at 400 °C is lower than that observed at 500 °C. Peaks corresponding to the appearance of Co_3O_4 are also not observed. The results obtained for higher temperatures are consistent with those available in the literature. The lack of identification of $SrCO_3$ should also be noted. At the same time, the use of an amorphous material causes its high variability because the diffractogram made after the tests for temperatures below 600 °C differs significantly from the one made before the tests. It seems that the material crystallises slowly, which may cause an initial large variability in the parameters describing the electrode. This may also explain the increase in polarisation resistance obtained during ageing measurements, and the observed increase in this parameter is due to changes occurring in the material and not to its degradation.

4. Electrode reaction mechanism on a partially-amorphous LSC oxygen electrode

The transport of charges at the oxygen electrode in MIEC (Mixed Ionic-Electronic Conductor) materials, such as LSC, proceeds through three steps: the adsorption of oxygen molecules followed by their dissociation, the reduction of oxygen ions leading to their ionisation, and the integration of oxygen ions into the surface of the oxygen electrode [53]. In the following step, the oxygen ion undergoes either bulk diffusion or surface diffusion, and ultimately, in the final step, it reaches the interface between the oxygen electrode and the electrolyte.

Amorphous or partially amorphous materials exhibit unique properties that allow for electrochemical enhancement and catalytic activity. These materials show a short-range order, but on a larger scale, along-range disorder should be considered. For those material a reduction of electronic conductivity, increase in the occurrence of defects and vacancies, and possible faster ionic diffusion is observed [54]. In amorphous or partially-amorphous material, the movement of oxygen occurs through a "saddle point" located between two A-site cations and one B-site cation, instead of directly jumping from one site to the adjacent vacancy along the anion octahedra edge. The larger volume of the perovskite cell in the amorphous oxygen electrode material, along with its lower density, may cause a decrease in the amount of energy required for oxygen to move into a neighbouring oxygen vacancy. Similarly, the pathway through which oxygen moves in an amorphous 'pre'-perovskite

MOST WIEDZY Downloaded from mostwiedzy.pl

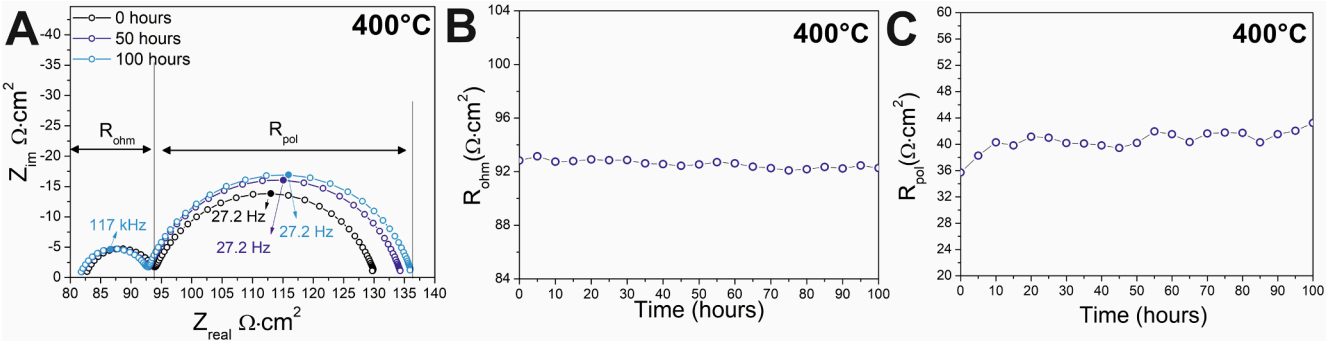

Fig. 6. Impedance spectra at 0, 50, and 100 h for a sample subjected to 100-hour ageing tests in 400 °C (A); change of ohmic resistance (B), and polarisation resistance during ageing measurements (C).

structure is likely to be distinct, resulting in a reduced activation energy for oxygen diffusion [55–57]. The combination of various sharing geometries also affects the properties. Amorphous materials are created by stacking distorted metal–oxygen polyhedra to create lattice arrays in a random arrangement. The oxygen atoms of multiple polyhedra are connected to each other through various sharing configurations, including edge sharing, corner sharing, and face sharing. The presence of extensive structural disturbances in amorphous materials reduces the mean free scattering path, while the absence of grain boundaries leads to the uniformity of electronic properties over large areas [54]. The improvement obtained in the catalytic properties of LSC in the partially amorphous form indicates that the greater number of defects and vacancies produced is responsible for this effect.

Annealing at 400 °C results in a reduction in polarisation resistance due to a high active surface area, a larger number of defects and vacancies, and extremely small grains, but at the same time increases ohmic resistance. Higher annealing temperatures lead to larger grain sizes, crystallisation of LSC, and a reduction in the number of defects and vacancies compared to the partially amorphous form. This outcome exhibits reduced ohmic resistance while also demonstrating notably higher polarisation resistance.

4.1. Literature comparison of electrochemical performance of oxygen electrodes at low temperatures

Among cited works an introduction part, for improve the discussion the result obtainsed in this study was compared with other works The obtained results were compared with the data available in the literature, not only for LSC but also for other promising oxygen electrode materials. Fig. 7A presents Arrhenius plots for cited works and a comparison with this work. Delving deeper into the topic, Fig. 7B presents the R_{pol} values obtained over the last 15 years. This chart also includes a division into the use of a single material and the composites.

For example Kamecki et al. describe the use of LSC oxygen electrode layer deposited with spray pyrolysis method. The electrode thickness was set as 400 nm. The symmetrical cell showed very low value of the polarisation resistance in 400 °C as ~10 Ω·cm^2. The fuel cell with this electrode show high stability over the long time of stability experiment (around 1000 h) [40]. Very promising results were also achieved in the work of Nicolett et al. where they studied a CGO-based cathode infiltrated by praseodymium oxide. The polarization resistance value was ~2 Ω·cm^2 at 400 °C[6]. Hu et al. described the use of $SrCo_{1-x}Sb_xO_{3-\delta}$ as a potential cathode. At 500 °C, the polarisation resistance for the $SrCo_{0.8125}Sb_{0.1875}O_{3-\delta}$ sample was ~1.7 Ω·cm^2. Additionally, this work demonstrated an improvement in CO_2 tolerance [7]. Samat et al. described the use of single-phase, submicron LSC synthesized via a polymeric complexation method as an oxygen electrode in proton-conducting fuel cells. Symmetric samples were sintered at 900 °C. EIS measurements at 400 °C showed an R_{pol} value of approximately 32 Ω·cm^2 [18]. Noh et al. prepared a cell with an LSC oxygen electrode approximately 1 μm thick. At a temperature of 400 °C, the ASR value was 17.7 Ω·cm^2 [58].

There are very few works describing the use of non-crystalline LSC. However, the comparison with them is the most meaningful. In the work of Cavallaro et al. a PLD-deposited layer with a thickness of approximately 300 nm was used and heat treated from room temperature to 750 °C, with an intermediate step at 200 °C. At a temperature of 415 °C, the R_{pol} value reached 850 Ω·cm^2 [20]. In a separate study, Evans et al. employed partially amorphous LSC as an oxygen electrode in micro-solid oxide fuel cells. They investigated electrode thicknesses of 100

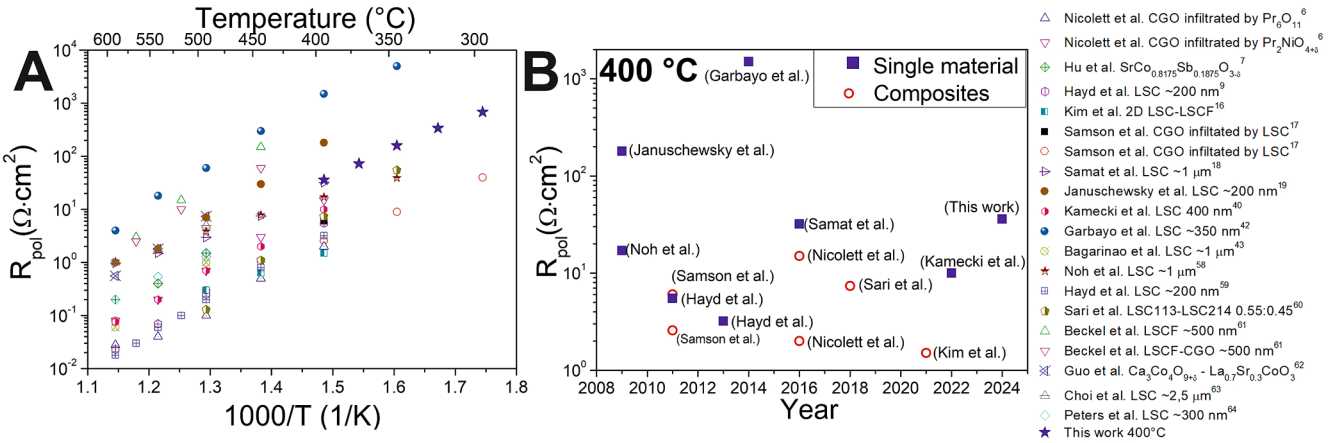

Fig. 7. Arrhenius plot of the polarization resistance of symmetrical half-cells in tests of cathodes that can be used in SOCs technology from literature data [6,7,9,16–19,40,42,43,58–64].

MOST WIEDZY Downloaded from mostwiedzy.pl

nm and 200 nm. For the 200 nm thickness at 400 °C, fuel cell measurements indicated an ASR value for the oxygen electrode not exceeding 0.3 $\Omega \cdot cm^2$ [12].

The values obtained in this work are in the middle of the polarization resistance values obtained in other works. This means that further development of partially amorphous oxygen electrode materials is needed. It is worth noting that in the case of single materials, better results are generally achieved with composites. Of the cited works, only one included temperature as low as 300 °C.

5. Conclusions

In this work, an oxygen electrode in the form of $La_{0.6}Sr_{0.4}CoO_{3-\delta}$ was deposited on $Ce_{0.8}Gd_{0.2}O_{2-\delta}$ pellets using the spin-coating technique. A new method for preparing the LSC precursor using UV radiation has been used. The structural analysis was based on tests such as XRD, HT-XRD, RAMAN spectra, FTIR, XANES, EXAFS, and WT as a function of annealing temperature in the range of 400–1000 °C. Electrochemical impedance spectroscopy allowed to determine the optimal range of oxygen electrode thickness (~500 nm) and to determine the optimal annealing temperature (400 °C).It has been shown that the partially amorphous LSC has significantly higher electrochemical activity. The partially amorphous nature of the material is indicated by the presence of characteristic bonds (typical for crystalline LSC, but lower intensity of the signal) with identified using Raman and FTIR spectroscopy. This is also indicated by the Bode characteristic in EIS measurements. Moreover, XRD and HT-XRD measurements indicate that the minimum crystallization temperature is approximately 600 °C (nanocrystalline).

The increase in electrochemical activity of partially amorphous LSC is probably due to the decreased oxidation state (from 3.4 to 2.9) of cobalt in partially amorphous LSC. This change is combined with a visibly lower coordination number of oxygen near the central atom. All this, combined with the irregular spatial structure, increases the number of defects in the material and oxygen vacancies.

Stability tests and post-mortem analysis of samples indicate adequate stability of the material combined with the lack of observations of oxides indicating material decomposition ($SrCO_3$ or Co_3O_4) indicate the potential use of partially amorphous LSC as an oxygen electrode in SOCs.

To the best of our knowledge, this work is the first to describe in a comprehensive study the electrochemical and structural properties of perovskite-based oxygen electrodes in SOC technology, focusing on such a low temperature. Attempts to describe partially amorphous material and demonstrate similarities and differences using multiple techniques are also worth noting.

CRediT authorship contribution statement

Bartłomiej Lemieszek: Writing – review & editing, Writing – original draft, Validation, Methodology, Investigation, Formal analysis, Data curation, Conceptualization. **Mindaugas Ilickas:** Writing – review & editing, Methodology, Investigation. **Jan Jamroz:** Writing – review & editing, Methodology, Investigation. **Asta Tamulevičienė:** Writing – review & editing, Methodology, Investigation. **Jakub Karczewski:** Writing – review & editing, Methodology, Investigation. **Patryk Błaszczak:** Writing – review & editing, Methodology, Investigation. **Alexey Maximenko:** Writing – review & editing, Supervision, Methodology, Investigation, Data curation. **Brigita Abakevičienė:** Writing – review & editing, Supervision, Methodology, Investigation. **Marcin Małys:** Writing – review & editing, Methodology, Investigation. **Sigitas Tamulevičius:** Writing – review & editing, Supervision, Resources, Methodology. **Piotr Jasiński:** Writing – review & editing, Supervision, Methodology. **Sebastian Molin:** Writing – review & editing, Supervision, Resources, Methodology, Data curation, Conceptualization.

Declaration of competing interest

The authors declare that they have no known competing financial interests or personal relationships that could have appeared to influence the work reported in this paper.

Data availability

Data will be made available on request.

Acknowledgements

This research has been supported by the National Science Centre (NCN) DAINA 2 project number UMO-2020/38/L/ST8/00513 and the Lithuanian Research Council (LMLT) project S-LL-21-8: “Porous metal supported micro-scale solid oxide fuel cells: fundamentals, fabrication and testing”. The XAFS measurements at ASTRA beamline at NSRC SOLARIS were made under the provision of the Polish Ministry and Higher Education project “Support for research and development with the use of research infra-structure of the National Synchrotron Radiation Centre SOLARIS” under contract Nr 1/SOL/2021/2. The further development of ASTRA beamline at NSRC SOLARIS was supported within the EU Horizon2020 program (952148-Sylinda).

Appendix A. Supplementary data

Supplementary data to this article can be found online at https://doi.org/10.1016/j.apsusc.2024.160620.

References

[1] A. Tarancón, Strategies for lowering solid oxide fuel cells operating temperature, Energies 2 (4) (2009) 1130–1150, https://doi.org/10.3390/en20401130.
[2] A. Alaswad, A. Baroutaji, A. Rezk, M. Ramadan, A.G. Olabi, Advances in Solid Oxide Fuel Cell Materials, Elsevier Ltd., 2021, https://doi.org/10.1016/B978-0-12-803581-8.11743-6.
[3] J.C.W. Mah, A. Muchtar, M.R. Somalu, M.J. Ghazali, Metallic interconnects for solid oxide fuel cell: a review on protective coating and deposition techniques, Int. J. Hydrogen Energy 42 (14) (2017) 9219–9229, https://doi.org/10.1016/J.IJHYDENE.2016.03.195.
[4] M.F. Vostakola, B.A. Horri, Progress in material development for low-temperature solid oxide fuel cells: a review, Energies 14 (5) (2021), https://doi.org/10.3390/en14051280.
[5] L. Yefsah, J. Laurencin, M. Hubert, et al., Electrochemical performance and stability of $PrO_{1.833}$ as an oxygen electrode for solid oxide electrolysis cells, Solid State Ion. 399 (March) (2023) 1–14, https://doi.org/10.1016/j.ssi.2023.116316.
[6] C. Nicollet, A. Flura, V. Vibhu, A. Rougier, J.M. Bassat, J.C. Grenier, An innovative efficient oxygen electrode for SOFC: Pr_6O_{11} infiltrated into Gd-doped ceria backbone, Int. J. Hydrogen Energy 41 (34) (2016) 15538–15544, https://doi.org/10.1016/j.ijhydene.2016.04.024.
[7] X. Hu, Y. Xie, Y. Wan, Y. Yang, X. Wu, C. Xia, Antimony-doped strontium cobalt oxide as promising cathode for low-temperature solid oxide fuel cell with excellent carbon dioxide tolerance, Appl. Catal. B Environ. 286 (2021) 119901, https://doi.org/10.1016/J.APCATB.2021.119901.
[8] Yi-Ching Chen, Masatomo Yashima, Takashi Ohta, Kenji Ohoyama, S. Yamamoto, Crystal Structure, Oxygen Deficiency, and Oxygen Diffusion Path of Perovskite-Type Lanthanum Cobaltites $La_{0.4}Ba_{0.6}CoO_{3-\delta}$ and $La_{0.6}Sr_{0.4}CoO_{3-\delta}$, J. Phys. Chem. C 116 (2012) 5246–5254.
[9] J. Hayd, H. Yokokawa, E. Ivers-Tiffée, Hetero-interfaces at nanoscaled (La, Sr) $CoO_{3-\delta}$ thin-film cathodes enhancing oxygen surface-exchange properties, J. Electrochem. Soc. 160 (4) (2013) F351–F359, https://doi.org/10.1149/2.017304jes.
[10] L. Dieterle, P. Bockstaller, D. Gerthsen, J. Hayd, E. Ivers-tiffée, Microstructure of nanoscaled $La_{0.6}Sr_{0.4}CoO_{3-\delta}$ cathodes for intermediate-temperature solid oxide fuel cells, Published Online (2011:) 249–258, https://doi.org/10.1002/aenm.201000036.
[11] J. Januschewsky, M. Kubicek, M. Stöger-Pollach, J. Bernardi, J. Fleig, Structural and chemical investigations of (La, Sr)$CoO_{3-\delta}$, Trans E C S Soc. Electrochem. 25 (2) (2009) 2397–2402, https://doi.org/10.1149/MA2009-02/12/1474.
[12] A. Evans, J. Martynczuk, D. Stender, C.W. Schneider, T. Lippert, M. Prestat, Low-temperature micro-solid oxide fuel cells with partially amorphous $La_{0.6}Sr_{0.4}CoO_{3-\delta}$ cathodes, Adv. Energy Mater. 5 (1) (2015) 1–9, https://doi.org/10.1002/aenm.201400747.
[13] M. Søgaard, P.V. Hendriksen, M. Mogensen, F.W. Poulsen, E. Skou, Oxygen nonstoichiometry and transport properties of strontium substituted lanthanum cobaltite, Solid State Ion. 177 (37–38) (2006) 3285–3296, https://doi.org/10.1016/J.SSI.2006.09.005.

MOST WIEDZY Downloaded from mostwiedzy.pl

[14] Y.T. Kim, N. Shikazono, Evaluation of electrochemical reaction mechanisms of $La_{0.6}Sr_{0.4}CoO_{3-\delta}$-$Gd_{0.1}Ce_{0.9}O_{2-\delta}$ composite cathodes by 3D numerical simulation, Solid State Ion. 319 (2018) 162–169, https://doi.org/10.1016/J.SSI.2018.02.014.

[15] R. Vinoth Kumar, A.P. Khandale, A review on recent progress and selection of cobalt-based cathode materials for low temperature-solid oxide fuel cells, Renew. Sustain. Energy Rev. 156 (2022) 111985, https://doi.org/10.1016/J.RSER.2021.111985.

[16] C. Kim, H. Lee, I. Jang, et al., Subcontinuous 2D $La_{0.6}Sr_{0.4}CoO_{3-\delta}$ nanosheet as an efficient charge conductor for boosting the cathodic activity of solid oxide fuel cells, Electrochim. Acta 366 (2021) 137371, https://doi.org/10.1016/j.electacta.2020.137371.

[17] A. Samson, M. Sogaard, R. Knibbe, N. Bonanos, High performance cathodes for solid oxide fuel cells prepared by infiltration of $La_{0.6}Sr_{0.4}CoO_{3-\delta}$ into Gd-Doped Ceria, J. Electrochem. Soc. 158(6) (2011), https://doi.org/10.1149/1.3571249.

[18] A. Abdul Samat, M.R. Somalu, A. Muchtar, O.H. Hassan, N. Osman, LSC cathode prepared by polymeric complexation method for proton-conducting SOFC application, J. Sol-Gel Sci. Technol. 78 (2) (2016) 382–393, https://doi.org/10.1007/s10971-015-3945-4.

[19] J. Januschewsky, M. Ahrens, A. Opitz, F. Kubel, J. Fleig, Optimized $La_{0.6}Sr_{0.4}CoO_{3-\delta}$ thin-film electrodes with extremely fast oxygen-reduction kinetics, Adv. Funct. Mater. 19 (19) (2009) 3151–3156, https://doi.org/10.1002/adfm.200900362.

[20] A. Cavallaro, P.C. Sherrell, E. Ware, A. Kilner, S.J. Skinner, Amorphous-cathode-route towards low temperature, Sust. Energy Fuels. 2 (2018) 862–875, https://doi.org/10.1039/c7se00606c.

[21] H. Funke, A.C. Scheinost, M. Chukalina, Wavelet analysis of extended x-ray absorption fine structure data, Phys Rev B - Condens Matter Mater Phys. 71 (9) (2005) 1–7, https://doi.org/10.1103/PhysRevB.71.094110.

[22] H. Funke, M. Chukalina, A.C. Scheinost, A new FEFF-based wavelet for EXAFS data analysis, J. Synchrotron Radiat. 14 (5) (2007) 426–432, https://doi.org/10.1107/S0909049507031901.

[23] T.H. Wan, M. Saccoccio, C. Chen, F. Ciucci, Influence of the discretization methods on the distribution of relaxation times deconvolution: implementing radial basis functions with DRTtools, Electrochim. Acta 184 (2015) 483–499, https://doi.org/10.1016/J.ELECTACTA.2015.09.097.

[24] M.P. Pechini, Method of Pre Parng Lead and Alkalne Earth Titanates and Nobates and Coat, US Pat 3,330,697. Published online 1967:2.

[25] M. Kim, D.H. Kim, G.D. Han, H.J. Choi, H.R. Choi, J.H. Shim, Lanthanum strontium cobaltite-infiltrated lanthanum strontium cobalt ferrite cathodes fabricated by inkjet printing for high-performance solid oxide fuel cells, J. Alloy. Compd. 843 (2020) 155806, https://doi.org/10.1016/J.JALLCOM.2020.155806.

[26] T. Yamamoto, Assignment of pre-edge peaks in K-edge x-ray absorption spectra of 3d transition metal compounds: electric dipole or quadrupole? Published Online (2008) 572–584, https://doi.org/10.1002/xrs.

[27] J. Choy, H. Jung, J. Yoon, N. Nanohybrid, N. Co-doped-sio, N.C. Sio, catalysis Co K-edge XAS study on a new cobalt, Published Online (2001) 599–601, https://doi.org/10.1107/S090904950001548X.

[28] F. De Groot, G. Vankó, P. Glatzel, The 1s x-ray absorption pre-edge structures in transition metal oxides, J. Phys. Condens. Matter 21 (10) (2009), https://doi.org/10.1088/0953-8984/21/10/104207.

[29] W.W. Zhang, E. Povoden-Karadeniz, Y. Shang, P.V. Hendriksen, M. Chen, Phase equilibria and defect chemistry of the La-Sr-Co-O system, J. Eur. Ceram. Soc. 43 (10) (2023) 4419–4430, https://doi.org/10.1016/j.jeurceramsoc.2023.03.026.

[30] X. Wang, Z. Pan, X. Chu, et al., Atomic-scale insights into surface lattice oxygen activation at the spinel/perovskite interface of $Co_3O_4/La_{0.3}Sr_{0.7}CoO_{3-\delta}$, Angew. Chem. 58 (2019) 11720–11725, https://doi.org/10.1002/anie.201905543.

[31] O. Celikbilek, A. Cavallaro, G. Kerherve, et al., Surface restructuring of thin-film electrodes based on thermal history and its significance for the catalytic activity and stability at the gas/solid and solid/solid interfaces, ACS Appl. Mater. Interf. 12 (30) (2020) 34388–34401, https://doi.org/10.1021/acsami.0c08308.

[32] A. Ishikawa, J. Nohara, S. Sugai, Raman study of the orbital-phonon coupling in $LaCoO_3$, Phys. Rev. Lett. 93 (13) (2004) 1–4, https://doi.org/10.1103/PhysRevLett.93.136401.

[33] N. Orlovskaya, D. Steinmetz, S. Yarmolenko, D. Pai, J. Sankar, J. Goodenough, Detection of temperature- and stress-induced modifications of $LaCoO_3$ by micro-Raman spectroscopy, Phys. Rev. B – Condens. Matter. Mater. Phys. 72 (1) (2005) 1–7, https://doi.org/10.1103/PhysRevB.72.014122.

[34] X. Li, Z. Peng, W. Fan, et al., Raman spectra study of nanocrystalline composite oxides, Mater. Chem. Phys. 46 (1) (1996) 50–54, https://doi.org/10.1016/0254-0584(96)80129-5.

[35] A.H. El, J.F. Pierson, M. Chaik, et al., Evolution of the structural, morphological, optical and electrical properties of reactively RF-sputtered cobalt oxide thin fi lms with oxygen pressure, Vacuum 2019 (159) (2018) 346–352, https://doi.org/10.1016/j.vacuum.2018.10.065.

[36] T. Ghorbani-Moghadam, A. Kompany, M. Golmohammad, The comparative study of doping Cu and Fe on the cathodic properties of $La_{0.7}Sr_{1.3}CoO_4$ layered perovskite compound: to be used in IT-SOFC, J. Alloy. Compd. 926 (2022) 166928, https://doi.org/10.1016/J.JALLCOM.2022.166928.

[37] T. Ghorbani-Moghadam, A. Kompany, M.M. Bagheri-Mohagheghi, M.E. Abrishami, Cobalt spin states investigation of Ruddlesden-Popper $La_{2-x}Sr_xCoO_4$, using X-ray diffraction and infrared spectroscopy, J. Magn. Magn. Mater. 465 (2018) 768–774, https://doi.org/10.1016/J.JMMM.2018.06.062.

[38] M. Sivakumar, M. Sakthivel, S.M. Chen, P. Veerakumar, L.S. Bin, Sol-gel synthesis of carbon-coated $LaCoO_3$ for effective electrocatalytic oxidation of salicylic acid, ChemElectroChem 4 (4) (2017) 935–940, https://doi.org/10.1002/celc.201600714.

[39] L. Garces, M. Lopez-Medina, K.P. Padmasree, et al., A parchment-like supercapacitor made with sustainable graphene electrodes and its enhanced capacitance by incorporation of the LaSrCoO 3 perovskite, ChemistrySelect 7 (36) (2022), https://doi.org/10.1002/slct.202202199.

[40] B. Kamecki, G. Cempura, P. Jasiński, S.-F. Wang, S. Molin, Tuning electrochemical performance by microstructural optimization of the nanocrystalline functional oxygen electrode layer for solid oxide cells, ACS Appl. Mater. Interf. 14 (51) (2022) 57449–57459, https://doi.org/10.1021/acsami.2c18951.

[41] K. Develos-bagarinao, O. Celikbilek, R.A. Budiman, et al., electrochemical performance and long-term, Published Online (2022) 2445–2459, https://doi.org/10.1039/d1ta07235h.

[42] I. Garbayo, V. Esposito, S. Sanna, et al., Porous $La_{0.6}Sr_{0.4}CoO_{3-\delta}$ thin film cathodes for large area micro solid oxide fuel cell power generators, J. Power Sources 248 (2014) 1042–1049, https://doi.org/10.1016/j.jpowsour.2013.10.038.

[43] K. Develos-Bagarinao, K. Yamaji, H. Kishimoto, H. Shimada, K. Yamaji, Nanoengineering of cathode layers for solid oxide fuel cells to achieve superior power densities, Nat. Commun. 12 (2021) 3979, https://doi.org/10.1038/s41467-021-24255-w.

[44] S.B. Adler, Factors governing oxygen reduction in solid oxide fuel cell cathodes, Chem. Rev. 104 (10) (2004) 4791–4843, https://doi.org/10.1021/cr020724o.

[45] C. Fu, K. Sun, N. Zhang, X. Chen, D. Zhou, Electrochemical characteristics of LSCF–SDC composite cathode for intermediate temperature SOFC, Electrochim. Acta 52 (13) (2007) 4589–4594, https://doi.org/10.1016/J.ELECTACTA.2007.01.001.

[46] T. Jacobsen, P.V. Hendriksen, S. Koch, Diffusion and conversion impedance in solid oxide fuel cells, Electrochim. Acta 53 (25) (2008) 7500–7508, https://doi.org/10.1016/J.ELECTACTA.2008.02.019.

[47] B.A. Boukamp, H.J.M. Bouwmeester, Interpretation of the Gerischer impedance in solid state ionics, Solid State Ion. 157 (2003) 29–33, https://doi.org/10.1016/S0167-2738(02)00185-6.

[48] A. Esquirol, N.P. Brandon, J.A. Kilner, M. Mogensen, Electrochemical characterization of $La_{0.6}Sr_{0.4}Co_{0.2}Fe_{0.8}O_{3-\delta}$ cathodes for intermediate-temperature SOFCs, J. Electrochem. Soc. 151 (2004) 1847–1855, https://doi.org/10.1149/1.1799391.

[49] A. Mroziński, S. Molin, J. Karczewski, T. Miruszewski, P. Jasiński, Electrochemical properties of porous $Sr_{0.86}Ti_{0.65}Fe_{0.35}O_3$ oxygen electrodes in solid oxide cells: impedance study of symmetrical electrodes, Int. J. Hydrogen Energy 44 (2018) 1827–1839, https://doi.org/10.1016/j.ijhydene.2018.11.203.

[50] B.A. Boukamp, A linear Kronig-Kramers transform test for immittance data validation, J. Electrochem. Soc. 142 (6) (1995) 1885–1894, https://doi.org/10.1149/1.2044210.

[51] M. Schönleber, D. Klotz, E. Ivers-Tiffée, A method for improving the robustness of linear kramers-kronig validity tests, Electrochim. Acta 131 (2014) 20–27, https://doi.org/10.1016/J.ELECTACTA.2014.01.034.

[52] T. Zhang, Y. Zhao, X. Zhang, et al., Thermal stability of an in situ exsolved metallic nanoparticle structured perovskite type hydrogen electrode for solid oxide cells, Published Online (2019), https://doi.org/10.1021/acssuschemeng.9b04350.

[53] A. Endo, H. Fukunaga, C. Wen, K. Yamada, Cathodic reaction mechanism of dense $La_{0.6}Sr_{0.4}CoO_{3-\delta}$ and $La_{0.81}Sr_{0.09}MnO_3$ electrodes for solid oxide fuel cells, Solid State Ion. 135 (1–4) (2000) 353–358, https://doi.org/10.1016/S0167-2738(00)00466-5.

[54] S. Yan, K.P. Abhilash, L. Tang, et al., Research advances of amorphous metal oxides in electrochemical energy storage and conversion, Small 15 (4) (2019) 1–30, https://doi.org/10.1002/smll.201804371.

[55] J.A. Kilner, R.J. Brook, A study of oxygen ion conductivity in doped non-stoichiometric oxides, Solid State Ion. 6 (3) (1982) 237–252, https://doi.org/10.1016/0167-2738(82)90045-5.

[56] M.S. Islam, M. Cherry, C.R.A. Catlow, Oxygen diffusion in $LaMnO_3$ and $LaCoO_3$ perovskite-type oxides: a molecular dynamics study, J. Solid State Chem. 124 (2) (1996) 230–237, https://doi.org/10.1006/JSSC.1996.0231.

[57] M. Cherry, M.S. Islam, C.R.A. Catlow, Oxygen ion migration in perovskite-type oxides, J. Solid State Chem. 118 (1) (1995) 125–132, https://doi.org/10.1006/JSSC.1995.1320.

[58] H. Noh, J. Son, H. Lee, H. Song, H.-W. Lee, J. Lee, Low temperature performance improvement of SOFC with thin film electrolyte and electrodes fabricated by pulsed laser deposition, J. Electrochem. Soc. 156 (12) (2009) B1484, https://doi.org/10.1149/1.3243859.

[59] J. Hayd, L. Dieterle, U. Guntow, D. Gerthsen, E. Ivers-Tiffée, Nanoscaled $La_{0.6}Sr_{0.4}CoO_{3-\delta}$ as intermediate temperature solid oxide fuel cell cathode: microstructure and electrochemical performance, J. Power Sources. 196 (17) (2011) 7263–7270, https://doi.org/10.1016/J.JPOWSOUR.2010.11.147.

[60] D. Sari, F. Piskin, Z.C. Torunoglu, B. Yasar, Y.E. Kalay, T. Ozturk, Combinatorial development of nanocrystalline/amorphous (La, Sr)CoO_3-(La, Sr)$_2CoO_4$ composite cathodes for IT-SOFCs, Solid State Ion. 326 (October) (2018) 124–130, https://doi.org/10.1016/j.ssi.2018.10.003.

[61] D. Beckel, U.P. Muecke, T. Gyger, G. Florey, A. Infortuna, L.J. Gauckler, Electrochemical performance of LSCF based thin film cathodes prepared by spray pyrolysis, Solid State Ion. 178 (2007) 407–415, https://doi.org/10.1016/j.ssi.2007.01.019.

MOST WIEDZY Downloaded from mostwiedzy.pl

[62] P. Guo, X. Huang, X. Zhu, et al., A new composite material $Ca_3Co_4O_{9+d}$+$La_{0.7}Sr_{0.3}CoO_3$ developed for intermediate-temperature SOFC cathode, Fuel Cells 13 (5) (2013) 666–672, https://doi.org/10.1002/fuce.201300031.
[63] S. Choi, S. Yoo, J. Shin, G. Kim, J.E. Soc, P. B-b, High Performance SOFC cathode prepared by infiltration of $La_{n+1}Ni_nO_{3n+1}$ (n = 1, 2, and 3) in porous YSZ high performance SOFC cathode prepared by infiltration, J. Electrochem. Soc. 158 (8) (2011) B995–B999, https://doi.org/10.1149/1.3598170.
[64] C. Peters, A. Weber, E. Ivers-tiffée, Nanoscaled „$La_{0.5}Sr_{0.5}CoO_{3-\delta}$ thin film cathodes for SOFC application at 500°C < T < 700°C, Published Online (2008:) 730–737, https://doi.org/10.1149/1.2909552.

MOST WIEDZY Downloaded from mostwiedzy.pl